Langmuir films of layered nanomaterials: edge interactions and cell culture applications

Article (Accepted Version)

B: Biomaterials and Membranes

Langmuir Films of Layered Nanomaterials: Edge Interactions and Cell Culture Applications

Rhiannon W. Harries, Christopher J. Brown, Sean P. Ogilvie, Matthew J. Large, Aline Amorim Graf, Keiran Clifford, Thomas Simon, Georgios Giamas, Alan B. Dalton, and Alice A. K. King

J. Phys. Chem. B, **Just Accepted Manuscript** • DOI: 10.1021/acs.jpcb.0c05573 • Publication Date (Web): 24 Jul 2020

Langmuir Films of Layered Nanomaterials:

Edge Interactions and Cell Culture Applications

Rhiannon W. Harries,[1] Christopher J. Brown,[1] Sean P. Ogilvie,[1] Matthew J. Large,[1]*

Aline Amorim Graf,[1] Keiran Clifford,[1] Thomas Simon,[2] Georgios Giamas,[2] Alan B. Dalton,[1]

Alice A. K. King[1]*

[1] Department of Physics and Astronomy, University of Sussex, Brighton, United Kingdom, BN1 9QH

[2] Department of Biochemistry and Biomedicine, University of Sussex, Brighton, United Kingdom, BN1 9QG

* Corresponding Authors:

Rhiannon Harries

Department of Physics and Astronomy, University of Sussex, Brighton, United Kingdom, BN1 9QH

E-mail: r.w.harries@sussex.ac.uk

Alice King

Department of Physics and Astronomy, University of Sussex, Brighton, United Kingdom, BN1 9QH

E-mail: alice.king@sussex.ac.uk

Phone: +44 (0)1273 678699

Abstract

The application of nanomaterials in technology is limited by challenges in their processing into macroscopic structures with reliable and scalable methods. Herein, it is demonstrated that using scalable fabrication methods such as liquid-phase exfoliation it is possible to produce dispersions of a wide variety of layered nanomaterials, including the first demonstration of boron nitride, with controllable and standardised size and thickness scaling. These can be used as-produced for Langmuir deposition, to create single layer films with tuneable density. Of particular importance, we show that the difference in edge chemistry of these materials dictates the film formation process, and therefore can be used to provide a generic fabrication methodology that is demonstrated for various layered nanomaterials, including graphene, boron nitride and transition metal dichalcogenides. We show that this leads to controllable cancer cell growth on graphene substrates with different edge densities but comparable surface coverage, which can be produced on a statistically relevant cell study amount. This opens up pathways for the generic fabrication of a range of layered nanomaterial films for various applications, towards a commercially viable film fabrication technology.

Introduction

Liquid-phase exfoliation is a process which has been shown to be the most effective way to produce large-scale yields of various layered nanomaterials, making it the most practical production technique available [1,2]. Layered nanomaterials incorporate a range of two-dimensional materials with a variety of different properties associated with them. Graphene is possibly the most well-known of these, having received much attention both in the academic sphere and also in public discourse. Since it was first isolated [3], its interesting mechanical,

electronic, optical and thermal properties have been studied extensively [4–7]. Further research has looked into these properties in other layered nanomaterials such as transition metal dichalcogenides (TMDs) [8–10], hexagonal boron nitride (BN) [11,12], and other exotic layered crystals [13–15].

These new materials could lead to many innovations. Two-dimensional materials can be utilised for such wide-ranging applications as electronics and optoelectronics [6,10,16], biomarker detection [17,18], and energy-related areas [19]. Liquid processing of two-dimensional layered nanomaterials is necessary to obtain dispersions suitable for Langmuir deposition; this is a well-known method of creating thin films, whereby a nanomaterial dispersion is spread on a liquid subphase [20,21].

The thin films produced by this method are two-dimensional, in the sense that they comprise a single layer of particles, i.e. they are only as thick as the thickness of the exfoliated layered nanomaterial used, and depending upon the parameters used varying from monolayer to multilayer. By use of a moveable barrier it is possible to vary the surface area of a Langmuir trough, and hence to compress a nanomaterial film. This technique gives simple control of film creation, with small quantities (mg m^{-2}) of material resulting in high material efficiency. This allows production of single layer particulate films with high surface coverages.

Control over thin film creation is therefore crucial as different applications may require different finely-tuned film properties [22]. Control over Langmuir film assembly would allow for generic scalable procedures for a range of materials dependent upon application requirements. By providing a framework for normalising for material interactions, it is possible to understand film densities for different layered nanomaterials, including boron nitride (the first time its Langmuir behaviour and deposition has been shown), graphene, MoS_2, and WS_2. This will be useful for various applications, including in biomaterials, where edge interactions play a critical role in

cellular growth and adhesion as well as the optimisation of the nanomaterial surface for functionalisation or surface interaction [23]. Moreover, sample substrates for biological studies must be able to be produced repeatably to allow for statistically significant trials. We demonstrate that the growth of glioblastoma cancer cells is significantly modified by the presence of graphene edges by comparing growth on films made from two different size graphene nanosheets (larger sheets, L-gra, and smaller sheets, S-gra). This is critical not only for the understanding of cancer growth, but also for developing novel, stable, synthetic substrate systems for cellular studies.

Experimental Section

Materials

BN powder (0.5 g, Aldrich Chemistry) was added to 20 mL of cyclohexanone (VWR Chemicals) and probe sonicated using a Sonics Vibracell VCX750 and ½-inch (13 mm) tip at 60% amplitude for 3 hours. The resulting dispersion was centrifuged for 25,000 *g* min using a Thermo Scientific Sorvall Legend X1. The supernatant was collected for further characterisation.

MoS_2 powder (0.41 g, Aldrich Chemistry) was added to 20 mL of cyclopentanone (VWR Chemicals) and probe sonicated using a Sonics Vibracell VCX750 and ½-inch (13 mm) tip at 60% amplitude for 1 hour. The resulting dispersion was centrifuged for 150,000 *g* min using a Thermo Scientific Sorvall Legend X1. The supernatant was discarded, and 20 mL of fresh cyclopentanone added. This was probe sonicated using a Sonics Vibracell VCX750 and ½-inch (13 mm) tip at 60% amplitude for 3 hours. The resulting dispersion was centrifuged for 25,000 *g* min using a Thermo Scientific Sorvall Legend X1. The supernatant was collected for further characterisation.

WS_2 powder (0.75 g, Aldrich Chemistry) was added to 30 mL of acetone (VWR Chemicals) and probe sonicated using a Sonics Vibracell VCX750 and ½-inch (13 mm) tip at 60% amplitude for 1 hour. The resulting dispersion was centrifuged for 150,000 *g* min using a Thermo Scientific Sorvall Legend X1. The supernatant was discarded, and 20 mL of fresh cyclopentanone added. This was probe sonicated using a Sonics Vibracell VCX750 and ½-inch (13 mm) tip at 60% amplitude for 3 hours. The resulting dispersion was centrifuged for 25,000 *g* min using a Thermo Scientific Sorvall Legend X1. The supernatant was collected for further characterisation.

The WS_2/acetone dispersion was centrifuged for 5,400,000 *g* min using a Thermo Scientific Sorvall Legend X1. The supernatant was discarded, and the solute redispersed in 5 mL of fresh cyclohexanone added to each centrifuge tube.

Graphene dispersions in cyclohexanone were processed as described in Large et al. [24]. Size-selected graphene dispersions were required. The dispersion was diluted 1:1 with cyclopentanone (Aldrich Chemistry) for the largest flake size (referred to as L-gra). Liquid cascade centrifugation [25] was used to obtain fractions of the original dispersion with different nanosheet size by extraction and re-centrifugation of the supernatant after each centrifugation step (Figure S1). Each time, this process leaves behind a solute that has an increasingly smaller average flake size. The dispersion to be size-selected for small flake size (referred to as S-gra) was further diluted 1:10 in cyclopentanone before centrifugation for 4,800,000 *g* min using a Thermo Scientific Sorvall Legend X1. The supernatant was collected for further characterisation.

Methods

Langmuir-Schaefer (L-S) deposition

A NIMA 102A Langmuir trough and NIMA surface pressure sensor (type PS4, serial no. 045) equipped with platinum Wilhelmy plate was used. Material dispersions were used to create thin films with varying surface coverages. The dispersion concentrations used ranged between 0.018–2.558 g/L (i.e. within the range typically produced by liquid-phase exfoliation), and the amounts deposited ranged between 100–900 µL. For film fabrication calibration, a range of surface pressures has been used (ranging from approximately 0.5–40 mN/m). To investigate quantitatively, a series of thin films of various materials were deposited by LS technique at varying pressures.

Optical microscopy

Optical microscopy was performed using an Olympus BX53M microscope with a 5× objective in bright field mode. The optical micrographs were pre-processed to crop the image down to the area of the cover slip only.

Optical images of the samples were required for calculation of surface coverage. Images were taken of large sample areas (at least half of each 18 mm × 18 mm sample) to allow a more accurate approximation of the film distribution over the whole sample.

Binary threshold method to determine film surface coverage

A two-step post-processing method was used. Firstly, the open-source ImageJ software [26] was used to run a binary threshold on the micrographs to separate the nanomaterial film from the substrate (example micrograph shown in Figure S2a, and corresponding threshold shown in

Figure S2b). Secondly, a custom Python script was written to automate the calculation for determining the fraction of nanomaterial present.

UV-visible spectroscopy

UV-visible spectroscopy measurements were performed using a Shimadzu UV-3600 Plus spectrophotometer. Liquid characterisation was performed using quartz cuvettes (Starna Scientific); solid characterisation was performed using a microscope slide holder.

Atomic force microscopy

Atomic force microscopy (AFM) measurements were performed using a Bruker Dimension Icon atomic force microscope system in PeakForce QNM mode.

AFM was performed on sparse Langmuir films of each material in order to obtain statistics on flake length, width, and layer number using NanoScope Analysis software. This allows flake area to be calculated. At least 100 flakes of each material were used to obtain reliable statistics.

Cell study

The cell line used for the cell study was U87 glioblastoma from the American Type Culture Collection. The study ran for 14 days, with observations made at day 3 and day 13, and images taken at day 4 and day 12 using an EVOS FLC imaging system (Life Technologies) at 20× magnification.

Results and Discussion

Dispersions of various nanomaterials were prepared in-house using liquid-phase exfoliation. These dispersions were used to perform Langmuir-Schaefer deposition. Langmuir films are created by dropping nanomaterial dispersion onto a water subphase; as the solvent evaporates, a

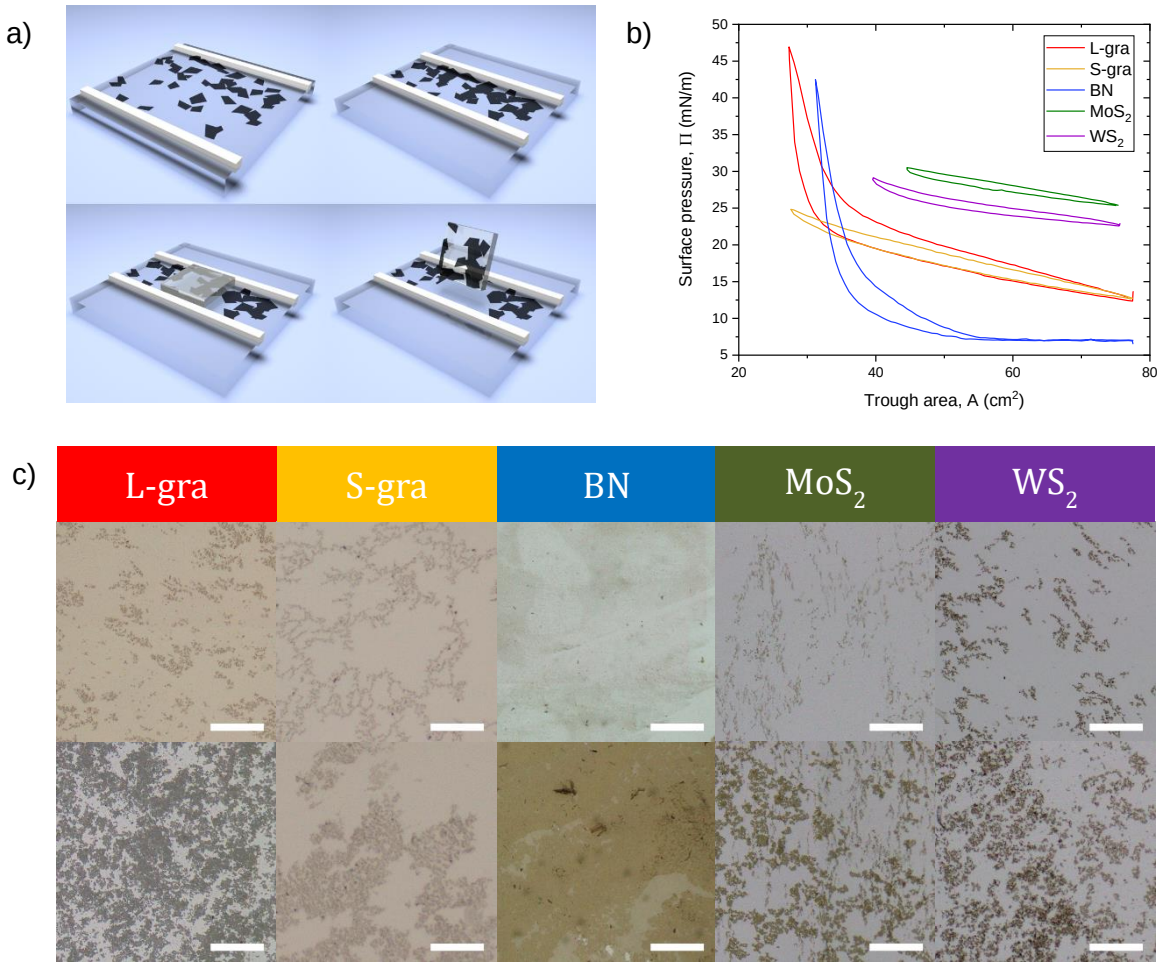

Figure 1a) Diagram showing the Langmuir-Schaefer deposition process. The deposited nanomaterial film is compressed with the trough barriers, then the substrate is brought into contact with the film before being lifted directly upwards (substrate parallel to air–water interface). Figure 1b) Pressure-area isotherms for each material used. Figure 1c) Optical micrographs for each material; the top row is of films deposited at a lower pressure (~10 mN/m), while the bottom row is of films deposited at a higher pressure (~25-30 mN/m). Images shown are small areas representative of the whole film. All scale bars = 100 µm.

thin, monolayer film is left at the air–water interface. Schaefer deposition is the horizontal lowering of a substrate to transfer this film [27], as shown in Figure 1a.

There are a few main requirements for solvents used for the Langmuir-Schaefer process. These include that the solvent has a high vapour pressure, so that it evaporates and leaves a film of particulates at the interface [28]; that the solvent spreads on the water surface, to maximize the area over which nanoparticles are spread to minimize reaggregation during solvent evaporation [29]; and that ideally, the dispersion should be water-immiscible.

Cycloketones such as cyclopentanone and cyclohexanone have been shown to be good solvents that satisfy all of these criteria [29]. Additionally, they have been shown to be good solvents for the exfoliation of layered nanomaterials [30,31]. This removes the need to exfoliate into a different solvent than that used for spreading, avoiding the extra step of redispersion of the material into a suitable spreading solvent. Moreover, redispersion is not always possible because generally good spreading solvents are not good for dispersion of two-dimensional layered nanomaterials, even if transferred [29]. By making use of these solvents, it is possible to process the nanomaterials from powder to completed Langmuir film in a single solvent, greatly simplifying the procedure, and providing the opportunity for bulk processing.

Typical area-pressure isotherms for all material monolayers with aqueous subphases used are given in Figure 1b. These isotherms show the 'phase transitions' [32] of the monolayer film. At low pressure (the gas phase) the material is sparsely distributed in the trough, creating 'films' which appear to be mostly blank substrate with islands of monolayer material. As the pressure increases and flakes of the material come into contact with each other (the liquid phase), the films become denser. This is more apparent in the isotherms for BN and the larger graphene flakes, where the pressure increases rapidly at smaller trough areas. The variance in behaviour for the different materials is discussed in more detail later. Once the nanomaterial film is at a given surface pressure, measured by use of a Wilhelmy plate, it is deposited onto a glass cover slip. Choosing a

range of surface pressures allowed films to range from those which were visibly dense and homogeneous to those which were visibly sparse.

Optical micrographs of typical films for each material after deposition at high and low pressures are shown in Figure 1c. It is clear that L-gra and BN differ from the other materials, as they have denser films. Although small sample areas are shown in Figure 1c, large film areas (of at least half of each 18 mm × 18 mm sample) were measured and used for the analysis. A simple, two-step post-processing method was used to determine the film surface coverage from the optical micrographs (shown in Figure S2).

The aim of this study is to develop a standardised method of creating films with known parameters using a scalable, commercially viable approach. To this end, the dispersions used were created using standard processes. These dispersions were characterised and shown to demonstrate universal (and expected) size scaling [33].

UV-visible spectroscopy measurements were performed on all dispersions, and representative spectra shown in Figure 2a. Metrics that make use of the absorbance feature ratios associated with each different material have been described in detail by Backes et al., and indicate the presence of exfoliated nanosheets [25,34–36]. This confirms the successful exfoliation to few-layer nanosheets. Lateral dimensions (length *L*, width *W*) of material nanosheets were measured by atomic force microscopy. Sheet thicknesses were measured from AFM profiles, and converted into layer number *N* using values for monolayer thicknesses from the literature for graphene [2], MoS_2 [35], WS_2 [25], and BN [36].

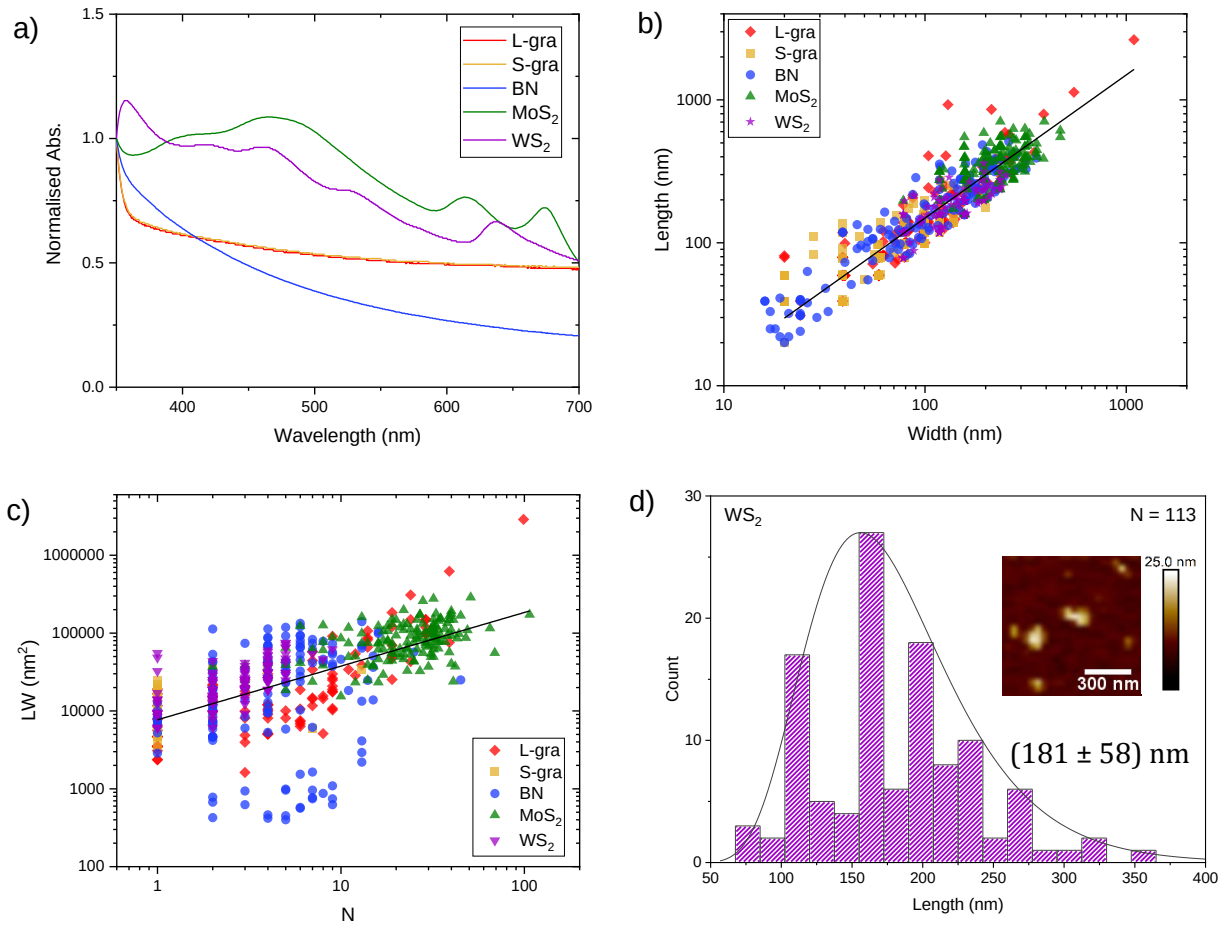

Figure 2a) UV-visible spectroscopy of nanomaterial dispersions used; absorbance normalised at 350 nm. Figure 2b) Nanosheet length vs width AFM statistics. Inset gives fit statistics. Figure 2c) Sheet-wise LW (length × width) vs layer number AFM statistics. Figure 2d) Plotted histogram for WS_2 length data, used to determine an average value <L> = (181 ± 58) nm. Inset shows AFM image of the material.

The *L* vs *W* scaling is given in Figure 2b and shows that while all nanosheets follow a power law scaling of the aspect ratio, length scales near linearly with width, i.e. constant aspect ratio. Table S1 gives aspect ratios for each material fitted individually, assuming a linear scaling. These aspect ratios imply that the shape is independent of the material, and suggests we can approximate the sheets as rectangles.

The product of length and width, *LW*, gives an approximation of nanosheet area. Plotting *LW* against *N* therefore shows how nanosheet area varies with number of layers. For liquid-exfoliated materials, the lateral size decreases as the thickness decreases; this is due to an increased sonication time leading to the creation of new edges [37,38]. Figure 2c shows that the materials used behave as expected. Moreover, all materials generally fall on a universal scaling, although BN shows some scatter. This is broadly consistent with other research into the effect of liquid-phase exfoliation on the size-thickness relationship [33]. There are some small differences between materials; results of fitting each material independently are shown in Table S2.

From Figure 2b, Figure 2c it is ascertained that all materials have a lateral size of less than 1 μm, and are all less than 30 layers thick on average (spread between 1 and 100 layers). Plotting histograms for each sample allows average values to be obtained by analysis of the distributions. Figure 2d shows a representative histogram and inset micrograph; additional histograms are available in the SI (Figure S3). All histograms are broadly log-normal, as expected [39,40]. The average values are consistent with the positions of clusters in the sheet-wise plots shown in Figure 2b, Figure 2c and are shown in Table 1. The average length and average number of layers are plotted in Figure S4.

Table 1) Average values for nanomaterial length, width, layer number, and approximate area, given with standard errors.

	$\langle L \rangle$ (nm)	$\sigma_{\langle L \rangle}$ (nm)	$\langle W \rangle$ (nm)	$\sigma_{\langle W \rangle}$ (nm)	$\langle N \rangle$	$\sigma_{\langle N \rangle}$	$\langle LW \rangle$ (nm^2)	$\sigma_{\langle LW \rangle}$ (nm^2)
L-gra	190	170	119	91	10	15	36000	89000
S-gra	89	49	63	36	2	1	7000	9000
BN	200	190	130	130	6	5	50000	160000
MoS_2	370	120	232	75	27	19	91000	56000
WS_2	181	58	139	47	3	2	27000	18000

The surface pressure of a film can change either through addition of more nanomaterial or by decreasing the trough area. For all materials, and a range of deposition pressures, surface pressure was plotted against surface coverage. Intuitively, the relation can be fitted logarithmically, as $\Pi \propto \log \Phi$. This implies that the denser the film, the slower the rate of change of pressure with respect to the surface coverage. This is represented mathematically by $\frac{d\Pi}{d\Phi} \propto \frac{1}{\Phi}$; i.e., once a film becomes dense, ever-greater increases in pressure are required to produce any further increases in surface coverage. This fit is shown in Figure 3a, and R^2 values are included in Table S3. Figure 3a shows that the materials behave as expected for a Langmuir process and can still be fitted effectively, despite the system being noisy due to factors such as transfer efficiency causing a scatter in data.

Although this basic relation works well, Fainerman et al. [41] describe a thermodynamic model for the interpretation of pressure-area isotherms of material monolayers. This also accounts for the size difference between material monolayers and solvent molecules. Their equation is

$$\Pi = -\frac{kT}{\omega_0}\left[ln\left(1-\frac{\omega}{A}\right)+\left(\frac{\omega}{A}\right)\right]-\Pi_{coh}, \quad (1)$$

where in the first term k is the Boltzmann constant, T is the temperature, ω_0 is the molecular area of a solvent molecule, ω is the molecular area of a nanoparticle, and A is the available surface area per nanoparticle.

The first term describes the increase in surface pressure with surface coverage due to entropy terms associated with subphase-nanosheet interactions. The offset term is the cohesion pressure, a term related to enthalpy, which describes long-range interactions between components [41]. In this study it is anticipated that these interactions will be dominated by attraction or repulsion

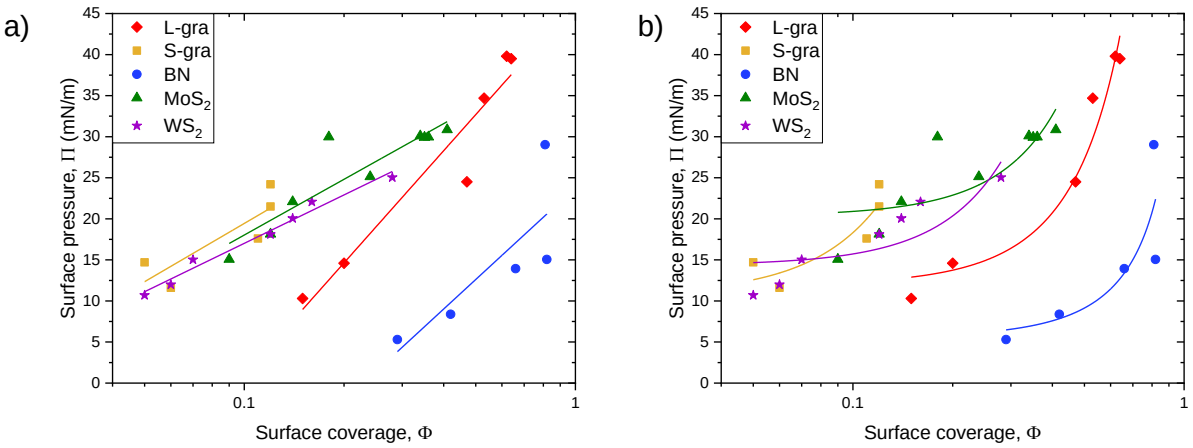

Figure 3a) Surface pressure versus surface coverage plot, fitted with a simple logarithm. Figure 3b) Surface pressure-surface coverage plot, fitted with Equation 1 [25].

between nanosheets when separated on the water surface, and based on the charge of edge states or van der Waals forces [42]. This information could suggest some phenomenon in the long-range interactions that is associated with the chemistry of materials used, leading to controlled film surface coverage.

The same surface pressure and surface coverage data are plotted in Figure 3b, but fitted with the model described in Equation 1. Although the model is designed for amphiphilic particles and only in the liquid expanded (low pressure) phase, the fit provides some insight for the layered nanomaterials and the intercept value at minimum pressure should hold true, with deviation expected for the higher pressure phases. The R^2 values are included in Table S3. As for the fitting in Figure 3a, although the fit is not ideal, presumably not capturing all of the complex edge interactions, it is an interesting start to capturing the dominant physics in what is a noisy and complex system that has not been previously described.

Values of Π_{coh} for each material are given in Table ***2***. Negative values of Π_{coh} indicate repulsive forces between the particles. This will be dominated by the edges rather than the surface, due to

the unique geometry of the L-S process. Higher interparticle forces lead to greater stability of films on the surface, because this creates a higher surface tension and therefore the films remain assembled without reorganisation or loss to the other phases [42]. Higher interparticle forces also lead to higher 2D film moduli, but will reduce the spreading efficiency of the nanomaterial at low density, and hence the optimisation of the surface coverage efficiency [43].

It is seen from Table ***2*** that BN has the least negative cohesion force and hence forms a film with the least pressure. This might correlate with the micrographs in Figure 1c, which show the BN films as being the densest and most uniform. Interestingly, it is still a slightly repulsive interparticle force, counter to bulk dispersion of BN which is usually described as attractive compared to other layered nanomaterials (although Π_{coh} = 0 mN/m is within error) [44]. However, as the edge effects dominate, the ionic nature of the BN bond leads to charged edges and potential for functionalised edge sites leading to dominant repulsive edges [45,44].

Table 2) Cohesion pressure values ($\boldsymbol{\Pi_{coh}}$) and uncertainties ($\boldsymbol{\sigma_{\Pi_{coh}}}$) for each material, as obtained from the fit in Figure 3b.

Material	Π_{coh} (mN/m)	$\sigma_{\Pi_{\mathrm{coh}}}$ (mN/m)
L-gra	-11.9	2.1
S-gra	-10.8	2.3
BN	-2.0	4.3
MoS_2	-20.3	2.1
WS_2	-14.3	1.6

For the exfoliation and size selection processes used in this experiment a broad range of size values were used, implying that pressure-area behaviour is not solely determined by either nanosheet size or material class. If only nanosheet size had any effect then Figure 3a, Figure 3b would show L-gra, BN, and WS_2 grouped together, with MoS_2 to one side of this cluster, and S-

gra to the other. If material class alone affected the pressure-area behaviour, then in Figure 3a, Figure 3b clear distinctions between the graphene, TMD, and BN samples are expected. In practice, S-gra and the two TMD samples are clustered together, with L-gra and BN separated, and the idea that behaviour might rely on a combination of nanosheet size and material class seems logical. Different material classes have different edge functionalities, which will influence film formation in different ways; however, size differences within material classes result in differing numbers of edges per unit area, and hence varying edge-edge interactions. If edge interactions between nanosheets play a significant role, as expected for L-S films, then this emphasises the need to account for nanosheet size before comparing the pressure-surface coverage data of the different samples. This would allow a fair comparison of how the intrinsic chemistry affects the edge-edge interaction between nanosheets.

As discussed previously, the influence of material edge interactions on the film surface pressure can be ascertained more easily by normalising the surface coverage, Φ, to nanosheet size. In particular, the need for a parameter that scales with the number of nanosheet edges per unit area is apparent. For this purpose, the centre-to-centre interparticle distance is used. This is derived in Appendix A (Supplementary Information), and has the form

$$s = \sqrt{\frac{\langle LW \rangle}{\Phi}}. \tag{2}$$

This new variable represents a normalisation of the surface coverage to account for the influence of the nanosheet size. Plotting surface pressure against this variable therefore represents a normalisation of the surface pressure-surface coverage plot. This is shown in Figure 4a, where it can be seen that this reduces the materials to two generic curves. The BN shows the closest

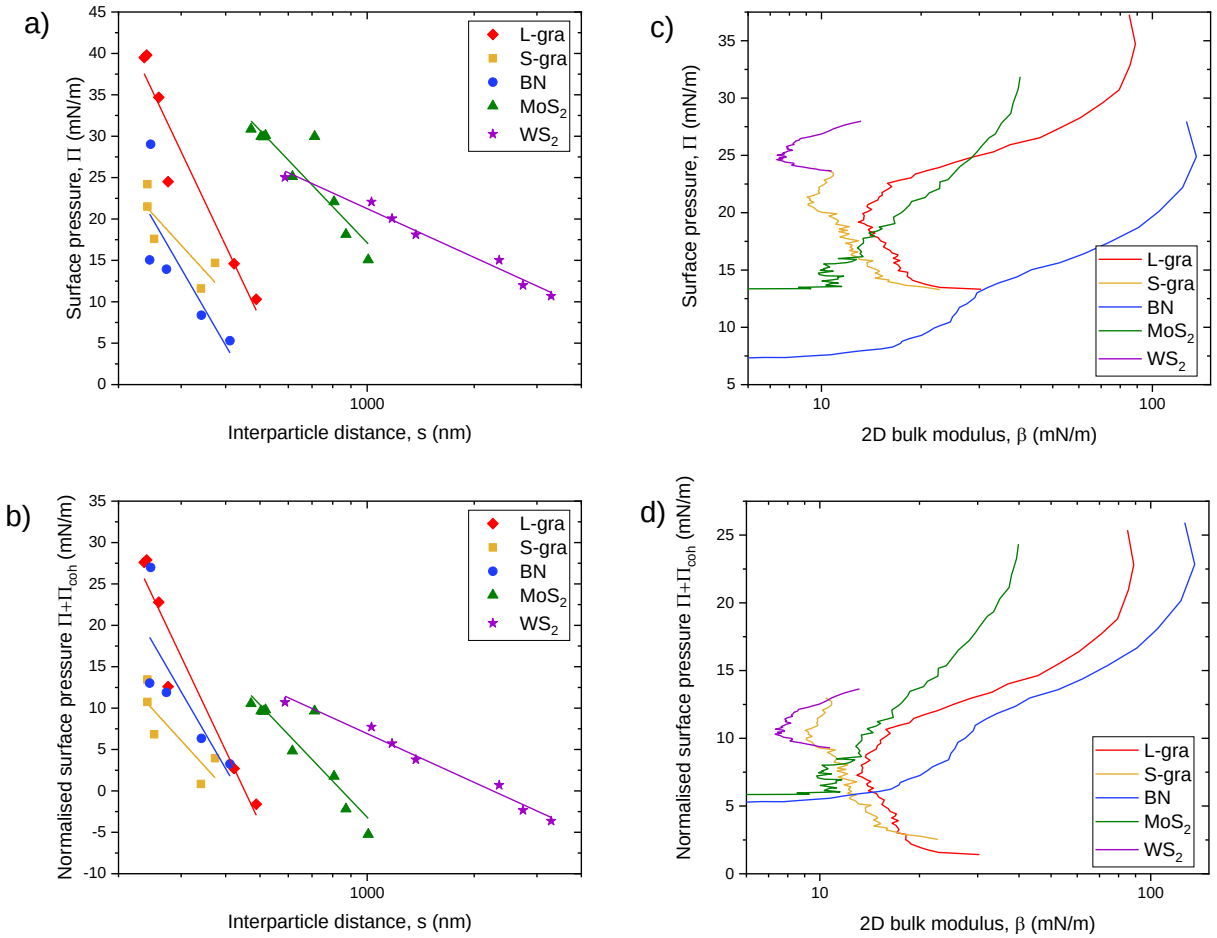

Figure 4a) Plot of surface pressure vs inverse interparticle distance. Figure 4b) Plot of normalised surface pressure vs inverse interparticle distance (y-axis normalised for cohesion pressure). Figure 4c) Plot of surface pressure vs 2D bulk modulus. Figure 4d) Plot of normalised surface pressure vs 2D bulk modulus (y-axis normalised for cohesion pressure).

particle approach, and densest film, as expected due to the stronger cohesion forces between the BN particles (Table ***2***).

If one normalises for the cohesion pressure determined from the fitting in Figure 3b, then in principle the long range interaction differences between the different materials is removed.

Indeed, it is seen in Figure 4b that the BN and graphene converge onto a single curve, but interestingly, the TMDs remain at a distance and with slightly lower slopes. The TMD films have the largest repulsion from the cohesion pressure (Table ***2***); this is expected because the sulfur-terminated edge sites are stable and so the charge distribution at the edge is uneven due the electronegativity difference between the sulfur and the metal [46,47]. This leads to highly polarised edges and therefore strong dipole interactions [46,47]. This effect is noted to be particularly strong for small particles as the edges become proportionally more dominant compared to the particle volume [48]. The WS_2 particles in this study are highly exfoliated and of small lateral dimensions, meaning they are likely to have a high degree of edge charge. This explains the strong repulsive cohesion pressure, but also the variation in the interparticle force compared to the other materials as seen in Figure 4. In addition to the long-range edge interactions, the MoS_2 in this experiment is particularly large, and multi-layered, so it is likely that there are large enough capillary forces acting on these particles compared to the WS_2 particles to start to affect the interactions [42]. The TMD films remain at a further interparticle separation compared to the other layered nanomaterials, due to their more polarised edge states and the comparatively stable nature of the edges. In this way, the class of material can be used to separate out the expected behaviour for monolayer film formation.

In nanomaterial films, rigidity percolation is reached when the particles form a connected bridge from one side of the Langmuir trough barrier to the other. For particles with the least repulsive edge interactions (such as BN) this bridge can form quickly, without total surface coverage, as even small numbers of particles agglomerate together forming branched networks. Conversely, a repulsive film will need to reach almost complete surface coverage to reach rigidity percolation ($\Phi = 0.7$) [49]. This is because the particles will continually rearrange on the subphase surface to

minimise their interaction, and therefore will spread out across the entire area until forced by density to form a rigid film. The 2D bulk modulus, β, is one way of quantifying this behaviour. This is described by

$$\beta = -A\left(\frac{\partial \Pi}{\partial A}\right)_T, \quad (3)$$

where A is the trough area, Π is the surface pressure, and T represents that the temperature is kept constant [49]. This is plotted for each material in Figure 4c. Although different material clearly have different maximum bulk moduli, the rigidity onset occurs at varying surface pressures.

However, when normalised to the cohesion pressure, the 2D bulk modulus follows a similar onset and maximisation (Figure 4d). This fits well with the concept of rigidity percolation. As expected, the BN has the largest 2D bulk modulus as it has the strongest interparticle interactions and the densest films. The TMDs show very weak modulus behaviours, as the repulsive edge states allow for particle slippage in the film system, maintaining a 'liquid-like' state for far longer, until geometrically 'jammed'. Therefore, the larger MoS_2 particles are locked into place more rapidly than the smaller WS_2 particles, or even the exceptionally small S-gra flakes.

This confirms that it is possible to extract interesting information about edge interactions from the cohesion pressure Π_{coh} only. This is a useful value beyond just Langmuir, providing insight into films more generally, including hybrid films, printing, heterostructure stitching, etc [50,51].

The process from Figure 2 to Figure 4 describes how variable pressure-surface coverage data can be normalised to nanosheet size to account for edge effects. This results in data clustered by material group that Equation 1 suggests is related to the area coverage when accounting for the

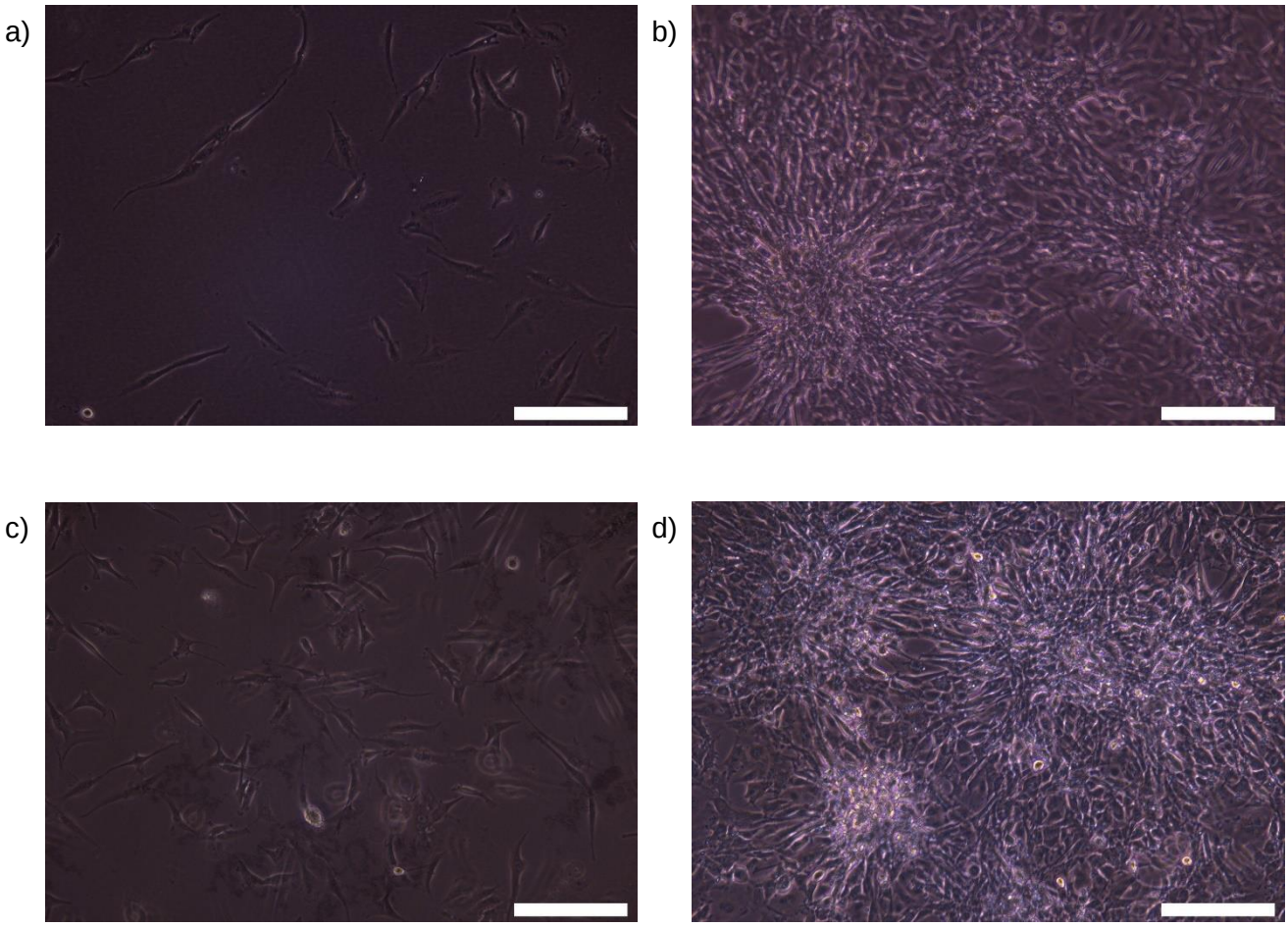

Figure 5) Optical micrographs showing U87 glioblastoma cell growth a) at 4 days on L-gra substrate, few cells present and not inclined to growth; b) at 12 days on L-gra substrate, still few proper cell clusters but those present were less confluent compared to other substrates; c) at 4 days on S-gra substrate, cells had good size extensions; d) at 12 days on S-gra substrate, many cell clusters observed and overconfluency apparent. All figures have scale bar = 200 μm.

area density of edges. Outstanding differences remaining in Figure 4 are due to the chemical nature of the edge functionalities and therefore merit study in further detail. Examining the edge chemistries in more detail should confirm the relative interaction strengths described above. However, even without knowing the detail of the chemistry it is possible to account for

nanomaterial class and size across a broad range of materials to determine film density from standard dispersion properties.

To demonstrate the importance of controlled film properties, a cell study comparing different edge densities was conducted. Two sets of films were produced from the same graphene dispersion size-selected to have larger and smaller sized nanosheets. As these films were deposited at similar surface coverages, the L-gra films had a lower area density of edges than the S-gra films.

It is observed that the edge density strongly determines the growth of glioblastoma cells (Figure 5). The films with greater edge density have greatly increased (~1.5 times greater) cell proliferation at 12 days compared to those with lower edge density, with increased cell cluster formation and improved cell spreading both at 4 and 12 days. This increased proliferation is likely due to the increased surface roughness that the cells experience with the greater edge density (as the graphene should itself be relatively inert), allowing them to form more adhesion sites. The cell stability is therefore increased, allowing more effective mobilisation and proliferation. Such a large impact on cell growth is critical when setting up controlled cell studies, and importantly this Langmuir substrate technique allows for the production of large quantities of identical substrates, which are important for the statistical requirements of biological studies [52].

Conclusions

Liquid-phase exfoliated dispersions of BN, MoS_2, WS_2, and two sizes of graphene were prepared and used to deposit Langmuir-Schaefer films at a range of different surface pressures. This is the first demonstration of the production of single layer BN films using this method. These

dispersions were made by generic processes to facilitate a standardised film creation method. UV-vis measurements showed the dispersions to be exfoliated, while AFM measurements were used to obtain average lateral dimensions and thicknesses for each material. Running a binary threshold on optical micrographs of the films gave quantitative values for the surface coverage of the material films, allowing the surface pressure-surface area relation to be plotted. To gain further insight from these plots, the data were normalised to account for differing sizes of nanosheets between materials. Plotting surface pressure against the interparticle distance begins to account for edge density effects and results in near parallel data. Additionally, the 2D bulk modulus was plotted, and, once normalised to the cohesion pressure, showed a similar rigidity onset and maximum for each material. Increased edge density on a graphene cell substrate increased colony formation and proliferation, demonstrating the importance, and tissue engineering potential, of control over film properties.

These results allow for an improved understanding of the physical and chemical influences on film formation, surface pressure, and surface coverage behaviour in Langmuir films of two-dimensional layered nanomaterials. This straightforward process has been demonstrated for a range of layered nanomaterials, including BN, which has not yet been used extensively for Langmuir deposition. An approach for analysis has been developed where size effects can be discarded, leaving only the effects due to the inherent chemistry of the material type. This combination of variable surface coverage and edge functionalities makes Langmuir films of layered nanomaterials interesting as substrate modifications for studies of cell growth and proliferation. These results will have uses beyond even cell studies, as this technique can be used to create films for a wide range of applications, such as transparent electrodes, supercapacitors,

etc. as well as providing a framework for processing new layered materials into single layer films, with maximised surface area.

References

(1) Nicolosi, V.; Chhowalla, M.; Kanatzidis, M. G.; Strano, M. S.; Coleman, J. N. Liquid Exfoliation of Layered Materials. *Science* **2013**, *340* (6139), 1226419. https://doi.org/10.1126/science.1226419.

(2) Paton, K. R.; Varrla, E.; Backes, C.; Smith, R. J.; Khan, U.; O'Neill, A.; Boland, C.; Lotya, M.; Istrate, O. M.; King, P.; et al. Scalable Production of Large Quantities of Defect-Free Few-Layer Graphene by Shear Exfoliation in Liquids. *Nat. Mater.* **2014**, *13* (6), 624–630. https://doi.org/10.1038/nmat3944.

(3) Novoselov, K. S.; Geim, A. K.; Morozov, S. V.; Jiang, D.; Zhang, Y.; Dubonos, S. V.; Grigorieva, I. V.; Firsov, A. A. Electric Field Effect in Atomically Thin Carbon Films. *Science* **2004**, *306* (5696), 666–669. https://doi.org/10.1126/science.1102896.

(4) Geim, A. K.; Novoselov, K. S. The Rise of Graphene. *Nat. Mater.* **2007**, *6* (3), 183–191. https://doi.org/10.1038/nmat1849.

(5) Castro Neto, A. H.; Guinea, F.; Peres, N. M. R.; Novoselov, K. S.; Geim, A. K. The Electronic Properties of Graphene. *Rev. Mod. Phys.* **2009**, *81* (1), 109–162. https://doi.org/10.1103/RevModPhys.81.109.

(6) Bonaccorso, F.; Sun, Z.; Hasan, T.; Ferrari, A. C. Graphene Photonics and Optoelectronics. *Nat. Photonics* **2010**, *4* (9), 611–622. https://doi.org/10.1038/nphoton.2010.186.

(7) Balandin, A. A. Thermal Properties of Graphene and Nanostructured Carbon Materials. *Nat. Mater.* **2011**, *10* (8), 569–581. https://doi.org/10.1038/nmat3064.

(8) Lee, K.; Kim, H.-Y.; Lotya, M.; Coleman, J. N.; Kim, G.-T.; Duesberg, G. S. Electrical Characteristics of Molybdenum Disulfide Flakes Produced by Liquid Exfoliation. *Adv. Mater.* **2011**, *23* (36), 4178–4182. https://doi.org/10.1002/adma.201101013.

(9) Eda, G.; Yamaguchi, H.; Voiry, D.; Fujita, T.; Chen, M.; Chhowalla, M. Photoluminescence from Chemically Exfoliated MoS2. *Nano Lett.* **2011**, *11* (12), 5111–5116. https://doi.org/10.1021/nl201874w.

(10) Wang, Q. H.; Kalantar-Zadeh, K.; Kis, A.; Coleman, J. N.; Strano, M. S. Electronics and Optoelectronics of Two-Dimensional Transition Metal Dichalcogenides. *Nat. Nanotechnol.* **2012**, *7* (11), 699–712. https://doi.org/10.1038/nnano.2012.193.

(11) Xu, M.; Liang, T.; Shi, M.; Chen, H. Graphene-Like Two-Dimensional Materials. *Chem. Rev.* **2013**, *113* (5), 3766–3798. https://doi.org/10.1021/cr300263a.

(12) Liu, L.; Feng, Y. P.; Shen, Z. X. Structural and Electronic Properties of H-BN. *Phys. Rev. B* **2003**, *68* (10), 104102. https://doi.org/10.1103/PhysRevB.68.104102.

(13) Zha, X.-H.; Yin, J.; Zhou, Y.; Huang, Q.; Luo, K.; Lang, J.; Francisco, J. S.; He, J.; Du, S. Intrinsic Structural, Electrical, Thermal, and Mechanical Properties of the Promising Conductor Mo2C MXene. *J. Phys. Chem. C* **2016**, *120* (28), 15082–15088. https://doi.org/10.1021/acs.jpcc.6b04192.

(14) Hantanasirisakul, K.; Gogotsi, Y. Electronic and Optical Properties of 2D Transition Metal Carbides and Nitrides (MXenes). *Adv. Mater.* **2018**, *30* (52), 1804779. https://doi.org/10.1002/adma.201804779.

(15) Zha, X.-H.; Zhou, J.; Zhou, Y.; Huang, Q.; He, J.; Francisco, J. S.; Luo, K.; Du, S. Promising Electron Mobility and High Thermal Conductivity in Sc2CT2 (T = F, OH) MXenes. *Nanoscale* **2016**, *8* (11), 6110–6117. https://doi.org/10.1039/C5NR08639F.

(16) Dean, C. R.; Young, A. F.; Meric, I.; Lee, C.; Wang, L.; Sorgenfrei, S.; Watanabe, K.; Taniguchi, T.; Kim, P.; Shepard, K. L.; et al. Boron Nitride Substrates for High-Quality Graphene Electronics. *Nat. Nanotechnol.* **2010**, *5* (10), 722–726. https://doi.org/10.1038/nnano.2010.172.

(17) Yoon, H. J.; Kim, T. H.; Zhang, Z.; Azizi, E.; Pham, T. M.; Paoletti, C.; Lin, J.; Ramnath, N.; Wicha, M. S.; Hayes, D. F.; et al. Sensitive Capture of Circulating Tumour Cells by Functionalized Graphene Oxide Nanosheets. *Nat. Nanotechnol.* **2013**, *8* (10), 735–741. https://doi.org/10.1038/nnano.2013.194.

(18) Singh, S.; Gill, A. A. S.; Nlooto, M.; Karpoormath, R. Prostate Cancer Biomarkers Detection Using Nanoparticles Based Electrochemical Biosensors. *Biosens. Bioelectron.* **2019**, *137*, 213–221. https://doi.org/10.1016/j.bios.2019.03.065.

(19) Luo, B.; Liu, S.; Zhi, L. Chemical Approaches toward Graphene-Based Nanomaterials and Their Applications in Energy-Related Areas. *Small* **2012**, *8* (5), 630–646. https://doi.org/10.1002/smll.201101396.

(20) Pockels, A. On the Spreading of Oil upon Water. *Nature* **1894**, *50* (1288), 223–224. https://doi.org/10.1038/050223a0.

(21) Langmuir, I. The Constitution and Fundamental Properties of Solids and Liquids. II. Liquids. *J. Am. Chem. Soc.* **1917**, *39* (9), 1848–1906. https://doi.org/10.1021/ja02254a006.

(22) Kalosi, A.; Demydenko, M.; Bodik, M.; Hagara, J.; Kotlar, M.; Kostiuk, D.; Halahovets, Y.; Vegso, K.; Marin Roldan, A.; Maurya, G. S.; et al. Tailored Langmuir–Schaefer Deposition of Few-Layer MoS2 Nanosheet Films for Electronic Applications. *Langmuir* **2019**, *35* (30), 9802–9808. https://doi.org/10.1021/acs.langmuir.9b01000.

(23) Solanki, S.; Soni, A.; Pandey, M. K.; Biradar, A.; Sumana, G. Langmuir–Blodgett Nanoassemblies of the MoS2–Au Composite at the Air–Water Interface for Dengue Detection. *ACS Appl. Mater. Interfaces* **2018**, *10* (3), 3020–3028. https://doi.org/10.1021/acsami.7b14391.

(24) Large, M. J.; Ogilvie, S. P.; Graf, A. A.; Lynch, P. J.; O'Mara, M. A.; Waters, T.; Jurewicz, I.; Salvage, J. P.; Dalton, A. B. Large-Scale Surfactant Exfoliation of Graphene and Conductivity-Optimized Graphite Enabling Wireless Connectivity. *Adv. Mater. Technol.* **2020**, 2000284. https://doi.org/10.1002/admt.202000284.

(25) Backes, C.; Szydłowska, B. M.; Harvey, A.; Yuan, S.; Vega-Mayoral, V.; Davies, B. R.; Zhao, P.; Hanlon, D.; Santos, E. J. G.; Katsnelson, M. I.; et al. Production of Highly Monolayer Enriched Dispersions of Liquid-Exfoliated Nanosheets by Liquid Cascade Centrifugation. *ACS Nano* **2016**, *10* (1), 1589–1601. https://doi.org/10.1021/acsnano.5b07228.

(26) Schneider, C. A.; Rasband, W. S.; Eliceiri, K. W. NIH Image to ImageJ: 25 Years of Image Analysis. *Nat. Methods* **2012**, *9*, 671–675. https://doi.org/10.1038/nmeth.2089.

(27) Langmuir, I.; Schaefer, V. J. Activities of Urease and Pepsin Monolayers. *J. Am. Chem. Soc.* **1938**, *60* (6), 1351–1360. https://doi.org/10.1021/ja01273a023.

(28) Fahimi, A.; Jurewicz, I.; Smith, R. J.; Sharrock, C. S.; Bradley, D. A.; Henley, S. J.; Coleman, J. N.; Dalton, A. B. Density Controlled Conductivity of Pristine Graphene Films. *Carbon* **2013**, *64*, 435–443. https://doi.org/10.1016/j.carbon.2013.07.096.

(29) Large, M. J.; Ogilvie, S. P.; King, A. A. K.; Dalton, A. B. Understanding Solvent Spreading for Langmuir Deposition of Nanomaterial Films: A Hansen Solubility

Parameter Approach. *Langmuir* **2017**, *33* (51), 14766–14771. https://doi.org/10.1021/acs.langmuir.7b03867.

(30) Hernandez, Y.; Lotya, M.; Rickard, D.; Bergin, S. D.; Coleman, J. N. Measurement of Multicomponent Solubility Parameters for Graphene Facilitates Solvent Discovery. *Langmuir* **2010**, *26* (5), 3208–3213. https://doi.org/10.1021/la903188a.

(31) Gao, Y.; Shi, W.; Wang, W.; Leng, Y.; Zhao, Y. Inkjet Printing Patterns of Highly Conductive Pristine Graphene on Flexible Substrates. *Ind. Eng. Chem. Res.* **2014**, *53* (43), 16777–16784. https://doi.org/10.1021/ie502675z.

(32) Schwartz, D. K. Langmuir-Blodgett Film Structure. *Surf. Sci. Rep.* **1997**, *27* (7), 245–334. https://doi.org/10.1016/S0167-5729(97)00003-4.

(33) Backes, C.; Campi, D.; Szydlowska, B. M.; Synnatschke, K.; Ojala, E.; Rashvand, F.; Harvey, A.; Griffin, A.; Sofer, Z.; Marzari, N.; et al. Equipartition of Energy Defines the Size–Thickness Relationship in Liquid-Exfoliated Nanosheets. *ACS Nano* **2019**, *13* (6), 7050–7061. https://doi.org/10.1021/acsnano.9b02234.

(34) Backes, C.; Paton, K. R.; Hanlon, D.; Yuan, S.; Katsnelson, M. I.; Houston, J.; Smith, R. J.; McCloskey, D.; Donegan, J. F.; Coleman, J. N. Spectroscopic Metrics Allow in Situ Measurement of Mean Size and Thickness of Liquid-Exfoliated Few-Layer Graphene Nanosheets. *Nanoscale* **2016**, *8* (7), 4311–4323. https://doi.org/10.1039/C5NR08047A.

(35) Backes, C.; Smith, R. J.; McEvoy, N.; Berner, N. C.; McCloskey, D.; Nerl, H. C.; O'Neill, A.; King, P. J.; Higgins, T.; Hanlon, D.; et al. Edge and Confinement Effects Allow *in Situ* Measurement of Size and Thickness of Liquid-Exfoliated Nanosheets. *Nat. Commun.* **2014**, *5*, 4576. https://doi.org/10.1038/ncomms5576.

(36) Griffin, A.; Harvey, A.; Cunningham, B.; Scullion, D.; Tian, T.; Shih, C.-J.; Gruening, M.; Donegan, J. F.; Santos, E. J. G.; Backes, C.; et al. Spectroscopic Size and Thickness Metrics for Liquid-Exfoliated *h*-BN. *Chem. Mater.* **2018**, *30* (6), 1998–2005. https://doi.org/10.1021/acs.chemmater.7b05188.

(37) Khan, U.; O'Neill, A.; Lotya, M.; De, S.; Coleman, J. N. High-Concentration Solvent Exfoliation of Graphene. *Small* **2010**, *6* (7), 864–871. https://doi.org/10.1002/smll.200902066.

(38) Xu, Y.; Cao, H.; Xue, Y.; Li, B.; Cai, W. Liquid-Phase Exfoliation of Graphene: An Overview on Exfoliation Media, Techniques, and Challenges. *Nanomaterials* **2018**, *8* (11). https://doi.org/10.3390/nano8110942.

(39) Alaferdov, A. V.; Gholamipour-Shirazi, A.; Canesqui, M. A.; Danilov, Yu. A.; Moshkalev, S. A. Size-Controlled Synthesis of Graphite Nanoflakes and Multi-Layer Graphene by Liquid Phase Exfoliation of Natural Graphite. *Carbon* **2014**, *69*, 525–535. https://doi.org/10.1016/j.carbon.2013.12.062.

(40) Kouroupis-Agalou, K.; Liscio, A.; Treossi, E.; Ortolani, L.; Morandi, V.; Pugno, N. M.; Palermo, V. Fragmentation and Exfoliation of 2-Dimensional Materials: A Statistical Approach. *Nanoscale* **2014**, *6* (11), 5926–5933. https://doi.org/10.1039/C3NR06919B.

(41) Fainerman, V. B.; Kovalchuk, V. I.; Lucassen-Reynders, E. H.; Grigoriev, D. O.; Ferri, J. K.; Leser, M. E.; Michel, M.; Miller, R.; Möhwald, H. Surface-Pressure Isotherms of Monolayers Formed by Microsize and Nanosize Particles. *Langmuir* **2006**, *22* (4), 1701–1705. https://doi.org/10.1021/la052407t.

(42) Bresme, F.; Oettel, M. Nanoparticles at Fluid Interfaces. *J. Phys. Condens. Matter* **2007**, *19* (41), 413101. https://doi.org/10.1088/0953-8984/19/41/413101.

(43) Cote, L. J.; Kim, F.; Huang, J. Langmuir−Blodgett Assembly of Graphite Oxide Single Layers. *J. Am. Chem. Soc.* **2009**, *131* (3), 1043–1049. https://doi.org/10.1021/ja806262m.

(44) Mohona, T. M.; Gupta, A.; Masud, A.; Chien, S.-C.; Lin, L.-C.; Nalam, P. C.; Aich, N. Aggregation Behavior of Inorganic 2D Nanomaterials Beyond Graphene: Insights from Molecular Modeling and Modified DLVO Theory. *Environ. Sci. Technol.* **2019**, *53* (8), 4161–4172. https://doi.org/10.1021/acs.est.8b05180.

(45) Liu, Y.; Bhowmick, S.; Yakobson, B. I. BN White Graphene with "Colorful" Edges: The Energies and Morphology. *Nano Lett.* **2011**, *11* (8), 3113–3116. https://doi.org/10.1021/nl2011142.

(46) Lin, Z.; McCreary, A.; Briggs, N.; Subramanian, S.; Zhang, K.; Sun, Y.; Li, X.; Borys, N. J.; Yuan, H.; Fullerton-Shirey, S. K.; et al. 2D Materials Advances: From Large Scale Synthesis and Controlled Heterostructures to Improved Characterization Techniques, Defects and Applications. *2D Mater.* **2016**, *3* (4), 042001. https://doi.org/10.1088/2053-1583/3/4/042001.

(47) Chhowalla, M.; Shin, H. S.; Eda, G.; Li, L.-J.; Loh, K. P.; Zhang, H. The Chemistry of Two-Dimensional Layered Transition Metal Dichalcogenide Nanosheets. *Nat. Chem.* **2013**, *5* (4), 263–275. https://doi.org/10.1038/nchem.1589.

(48) Silva, A. C. H. D.; Caturello, N. A. M. S.; Besse, R.; Lima, M. P.; Silva, J. L. F. D. Edge, Size, and Shape Effects on WS2, WSe2, and WTe2 Nanoflake Stability: Design Principles from an Ab Initio Investigation. *Phys. Chem. Chem. Phys.* **2019**, *21* (41), 23076–23084. https://doi.org/10.1039/C9CP03698A.

(49) Gopal, A.; Lee, K. Y. C. Headgroup Percolation and Collapse of Condensed Langmuir Monolayers. *J. Phys. Chem. B* **2006**, *110* (44), 22079–22087. https://doi.org/10.1021/jp061562t.

(50) Li, H.; Li, P.; Huang, J.-K.; Li, M.-Y.; Yang, C.-W.; Shi, Y.; Zhang, X.-X.; Li, L.-J. Laterally Stitched Heterostructures of Transition Metal Dichalcogenide: Chemical Vapor Deposition Growth on Lithographically Patterned Area. *ACS Nano* **2016**, *10* (11), 10516–10523. https://doi.org/10.1021/acsnano.6b06496.

(51) Winter, A.; George, A.; Neumann, C.; Tang, Z.; Mohn, M. J.; Biskupek, J.; Masurkar, N.; Reddy, A. L. M.; Weimann, T.; Hübner, U.; et al. Lateral Heterostructures of Two-Dimensional Materials by Electron-Beam Induced Stitching. *Carbon* **2018**, *128*, 106–116. https://doi.org/10.1016/j.carbon.2017.11.034.

(52) Hirsch, C.; Schildknecht, S. In Vitro Research Reproducibility: Keeping Up High Standards. *Front. Pharmacol.* **2019**, *10*. https://doi.org/10.3389/fphar.2019.01484.

Table of Contents (TOC) Image

Actual size

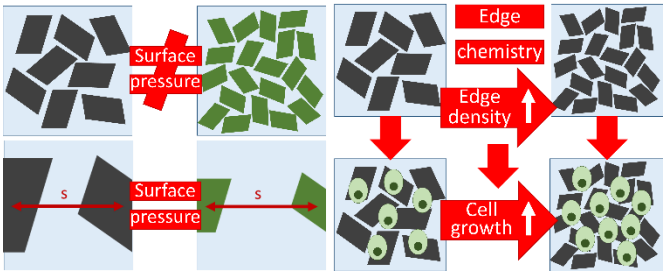

Larger version